Short-term stability of a microcell optical reference based on the Rb atom two-photon transition at 778 nm

Martin Callejo[1,*], **Andrei Mursa**[1], **Rémy Vicarini**[1], **Emmanuel Klinger**[1], **Quentin Tanguy**[1], **Jacques Millo**[1], **Nicolas Passilly**[1], **and Rodolphe Boudot**[1]

[1] *FEMTO-ST, CNRS, Université de Franche-Comté, ENSMM, 26 chemin de l'Epitaphe 25030 Besançon Cedex, France*
[*] *Corresponding author: rodolphe.boudot@femto-st.fr*

Compiled December 20, 2024

We report on the development and short-term stability characterization of an optical frequency reference based on the spectroscopy of the rubidium two-photon transition at 778 nm in a microfabricated vapor cell. When compared against a 778 nm reference signal extracted from a frequency-doubled cavity-stabilized telecom laser, the short-term stability of the microcell frequency standard is 3.5 × 10^{-13} $\tau^{-1/2}$ until 200 s, in good agreement with a phase noise level of + 43 dBrad^2/Hz at 1 Hz offset frequency. The two main contributions to the short-term stability of the microcell reference are currently the photon shot noise and the intermodulation effect induced by the laser frequency noise. With still a relevant margin of progress, these results show the interest of this spectroscopic approach for the demonstration of high-stability miniaturized optical vapor cell clocks. Such clocks are poised to be highly beneficial for applications in navigation, communications, and metrology.

http://dx.doi.org/10.1364/ao.XX.XXXXXX

---

1. INTRODUCTION

About twenty years ago, the advent of microfabricated alkali vapor cells [1], combined with low-power and high-bandwidth vertical-cavity surface emitting-lasers (VCSELs) [2], enabled the demonstration of the first microfabricated atomic clock [3]. The physics package of this microwave clock, based on coherent population trapping (CPT) [4, 5], had a volume of 9.5 mm^3, consumed 75 mW, and demonstrated a fractional frequency stability of 2.5 × 10^{-10} $\tau^{-1/2}$ up to 30 seconds (τ being the integration time), and of 2 × 10^{-9} at 10^4 s.

Following this prototype, intense research efforts were undertaken to enhance the performances of these clocks, including the development of VCSELs tuned on the alkali D_1 line [6–9], MEMS cell technologies with improved internal atmosphere [10–18], low noise and low power electronics [19], or integrated clock physics packages [20, 21].

These advances resulted in the emergence of commercially-available chip-scale atomic clocks (CSACs) with a volume of 15-20 cm^3, a power consumption lower than 150 mW, and a timing error of a few microseconds at 1 day [22]. These clocks are now deployed for underwater sensing, navigation systems, or secure and jam-resistant communications.

More recently, prototype microcell CPT clocks have showcased frequency stability levels in the low 10^{-12} range at 1 day [23–25] thanks to advanced light-shift compensation techniques [24, 26] and microcells built with low gas permeation glass windows [27–29].

Other approaches have also been explored for the advent of miniaturized microwave clocks with enhanced stability. A microcell clock based on the pulsed optically pumped (POP) technique [30] was demonstrated in [31] with a stability of 1.5 × 10^{-11} at 1 s and in the low 10^{-12} range at 1 day. In [32], a chip-scale beam microwave clock was reported with a stability of 1.2 × 10^{-9} $\tau^{-1/2}$, averaging down until 250 s.

A stimulating approach for demonstrating miniature clocks with significantly enhanced short-term stability consists of interrogating optical transitions in a microfabricated vapor cell, instead of microwave transitions. In this context, sub-Doppler spectroscopy techniques, based on the interaction of hot alkali atoms with two counter-propagating beams provided by a single laser source, are particularly attractive due to their extreme simplicity.

Saturated absorption spectroscopy (SAS) in a Rb microcell was reported in [33] using a Distributed Bragg Resonator (DBR) laser, yielding a frequency stability below 10^{-11} up to 10^4 s. A compact optical module, with a volume of 35 cm^3, a weight of 35 g, and a power consumption of 780 mW, was also demonstrated with SAS using a small-size glass-blown cell [34]. Piloted by embedded FPGA electronics, this reference reached a fractional frequency stability of 1.7 × 10^{-12} at 1 s and 6 × 10^{-12} at 10^5 s [35]. Dual-frequency sub-Doppler spectroscopy (DFSDS) [36, 37], that relies on a setup comparable to SAS but using a dual-frequency optical field, demonstrated, when applied to a Cs microcell with an external-cavity diode laser (ECDL), stability performances of 3 × 10^{-13} at 1 s and below 5 × 10^{-14} at 100 s [38]. Nevertheless, DFSDS requires the generation of a microwave-modulated laser, thereby introducing greater complexity to the optical setup architecture.

With a natural linewidth of about 330 kHz, the two-photon transition $5S_{1/2} \rightarrow 5D_{5/2}$ of the Rb atom at 778 nm constitutes an attractive option [39]. In this scheme, shown as an inset in Fig. 1, Rb atoms are excited to the $5D_{5/2}$ state by means of the simultaneous absorption of two 778.1 nm photons and then decay back to the ground state via the $6P_{3/2}$ state, emitting in the process blue photons at 420.2 nm. The blue fluorescence intensity is proportional to the 778.1 nm two photon absorption (TPA) and is then used to detect the sub-Doppler resonance peaks of rubidium. The presence of an intermediate $5P_{3/2}$ energy level close to the mid-point between the ground and excited levels increases the single-color two-photon absorption rate. This effect increases the signal-to-noise ratio (SNR) of the resonance signal, making this single-color approach a viable alternative to the complex, yet more efficient, 780 nm - 776 nm two-color absorption scheme [40, 41]. The Rb two-photon absorption at 778 nm has been successfully used for the demonstration of vapor cell-based optical clocks with stability levels in the low 10^{-13} range at 1 s and averaging down in the 10^{-15} range [42, 43]. A microcell optical clock operating on the Rb 778 nm TPA was demonstrated first at NIST [44]. A compact reference using a DBR laser was later reported with an Allan deviation of 2.8 × 10^{-12} at 1 s and approaching the 10^{-13} level after a few 100 s [45]. Using a low noise ECDL and a more favorable line of the ^{85}Rb isotope, this approach provided a stability of 1.8 × 10^{-13} at 1 s and approaching the 10^{-14} level after a few 100 s [46].

In this work, we report on the development and short-term stability characterization of a microcell optical frequency reference based on the Rb two-photon absorption at 778 nm. Our system employs a similar spectroscopic approach to [46]. However, we use the $5S_{1/2}(F = 2) \rightarrow 5D_{5/2}(F = 4)$ transition of the ^{87}Rb isotope for stabilization instead, and we feature a different MEMS cell architecture and laser source. Detailed spectroscopic and noise characterizations, useful for the analysis of short-term stability, are also reported. Measured against a 778 nm signal extracted from a cavity-stabilized laser, the optical standard offers an Allan deviation of 3.5 × 10^{-13} at 1 s, in good agreement with a laser phase noise of + 43 dBrad^2/Hz at 1 Hz Fourier frequency, and averaging down to 2 × 10^{-14} at 200 s. The main limitation to the microcell reference short-term stability is currently the photon shot noise, explained by the limited number of blue photons collected at the detector. The contribution of the intermodulation effect [47], induced by the laser frequency noise, is estimated at the level of 1 × 10^{-13} at 1 s. These results confirm the potential of this spectroscopic approach for the development of high-stability microcell optical standards. The analysis of the short-term noise budget also indicates a considerable room for stability improvement of such microcell optical references.

2. EXPERIMENTAL SETUP

Figure 1 shows a schematic of the experimental setup. The microcell optical reference consists of an ECDL, stabilized to the $5S_{1/2}(F_g = 2) \rightarrow 5D_{5/2}(F_e = 4)$ two-step transition of rubidium at 778.1 nm. A Faraday optical isolation stage in front of the laser reduces optical feedback. An acousto-optic modulator (AOM) is then used for the tuning and stabilization of the total laser power [48], independently of the laser bias current. For this purpose, a fraction of the laser beam is directed through a

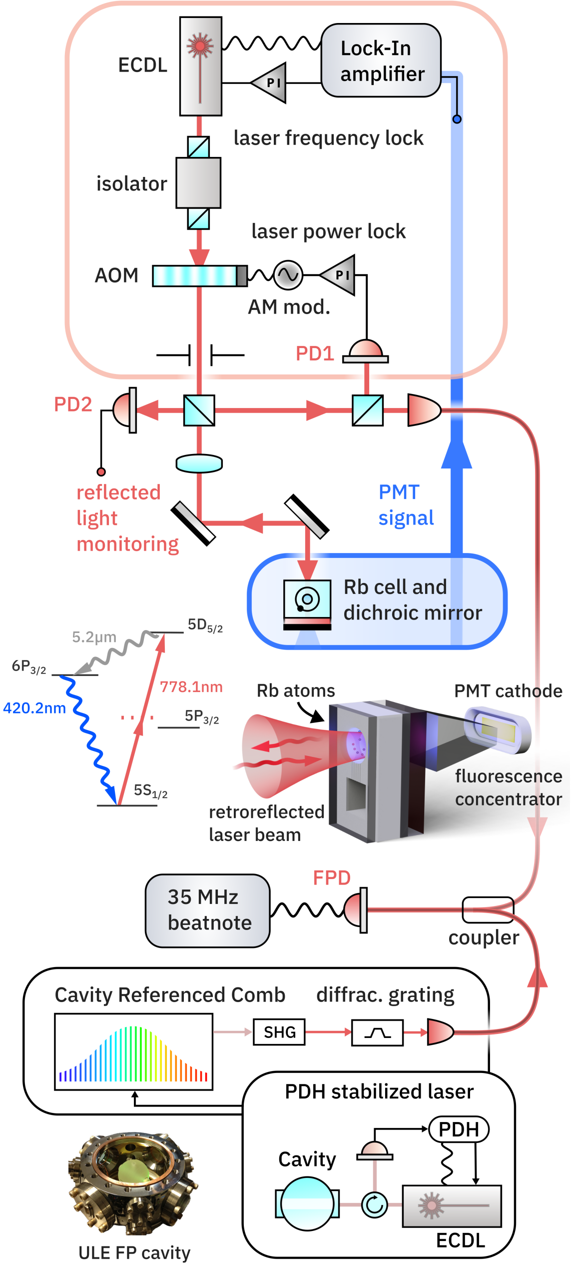

Fig. 1. Experimental setup. An ECDL is frequency stabilized to the 778.1 nm two-photon absorption of the Rb atoms in a microfabricated vapor cell. After the excitation of the $5S_{1/2} \rightarrow 5D_{5/2}$ transition, atoms decay to the ground state via radiative decay, emitting 420 nm fluorescence which is then collected by a photomultiplier tube (PMT). An acousto-optic modulator (AOM) is used to control and stabilize the laser power at the microcell input. A fraction of the locked laser light is injected into a fiber to be compared to the ultra-stable 778 nm signal extracted from a frequency-doubled frequency comb disciplined to a Ultra-Low-Expansion Fabry-Perot (ULE FP) cavity-stabilized laser. The final beatnote, obtained at about 35 MHz, is then analyzed using a frequency counter or phase noise analyzer. PD: photodiode. FPD: fast photodiode.

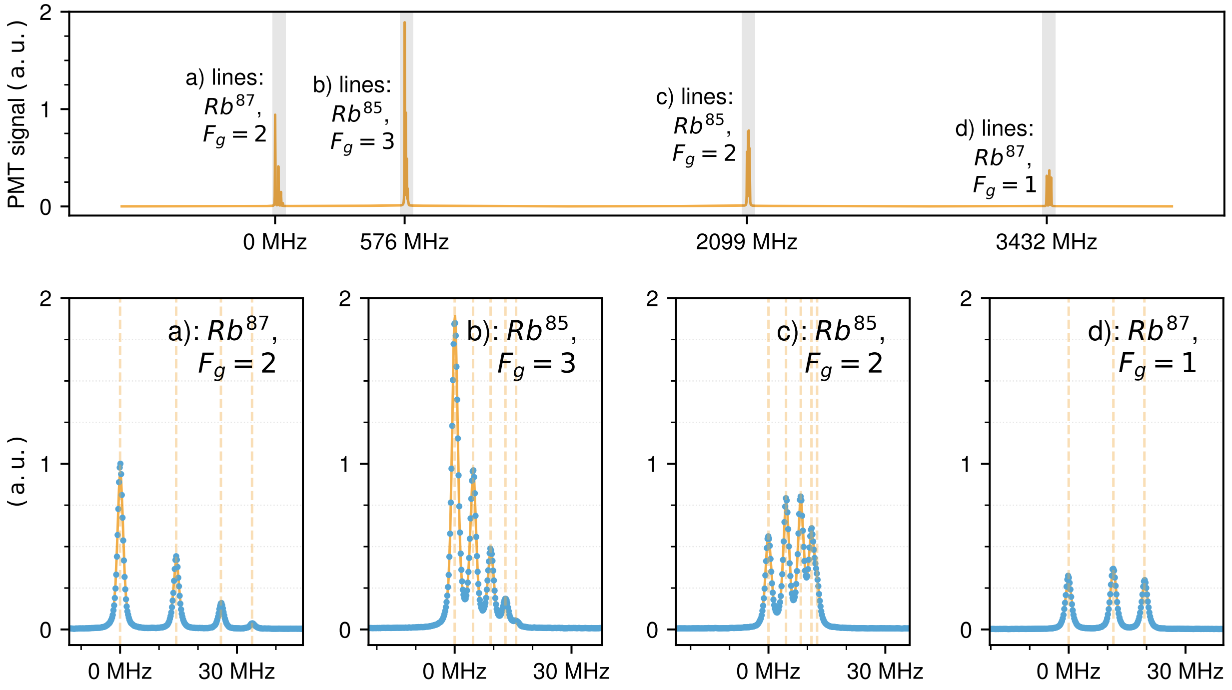

Fig. 2. Sub-Doppler spectroscopy of the $5S_{1/2} \to 5D_{5/2}$ transition at 778 nm of the Rb atoms in the microfabricated cell. The most intense peak is the $5S_{1/2}(F=3) \to 5D_{5/2}(F=5)$ transition of ^{85}Rb atom (peak on the left of sub-plot (b)). However, its proximity with neighboring lines made its use for the laser lock not robust enough. In this work, we used the $5S_{1/2}(F=2) \to 5D_{5/2}(F=4)$ transition of ^{87}Rb atom (leftmost peak in sub-plot (a)). For each sub-plot on the bottom, which zooms on the hyperfine structure of ^{87}Rb and ^{85}Rb lines, the first peak on the left was arbitrarily fixed to a null laser frequency detuning.

beam-splitter cube onto a photodiode (PD1). The output signal of this photodiode is compared to a voltage reference in order to produce an error signal. This signal is then fed to a proportional-integral (PI) controller that adjusts the amplitude of the RF signal used to drive the AOM. Most of the laser power at the output of the AOM (~12 mW) is sent to a physics package that houses a microfabricated Rb vapor cell, complete with temperature regulation and mu-metal magnetic shielding. We name the total laser power at the cell input P_l. A second out-of-loop photodiode (PD2) measures the power of the reflected laser beam. This photodiode is sensitive to transmission losses in the vapor cell, as the laser beam is transmitted through the cell windows twice before reaching it. These transmission losses directly influence the intensity of the light in the vapor cell, potentially contributing to light shift effects. Initially, one of the main motivations for using PD2 was to detect possible losses due to rubidium condensation on the cell windows. However, no conclusive results have been obtained to date from this out-of-loop photodiode, as the relatively small detected intensity fluctuations were not correlated with the measured frequency fluctuations.

The MEMS cell fabrication followed the processes described in [13, 17], yet no buffer gas was introduced before the cell sealing. The cell consists of two neighboring cavities, structured in silicon using deep-reactive ion etching (DRIE), and sandwiched between two anodically-bonded 500 μm-thick borosilicate glass windows. A pre-embedded Rb pill-dispenser alloy, laser-activated after final sealing of the cell, is used to fill the cell with Rb vapor (natural isotopic abundance). The cavity in which atom-light interaction takes place has a diameter of 2 mm and a length of 1.5 mm. The cell can be temperature-stabilized at set-points ranging from 70 to 120°C. A plano-convex lens (f = 100 mm), placed in front of the cell, is used to focus the laser beam so that the waist of the laser beam ($w_0 \sim 100$ μm) is located at the surface of a dichroic mirror located on the backside of the cell. This lens-mirror arrangement ensures a high light intensity in the cell and the overlapping of counter-propagating laser beams for Doppler broadening suppression. The mirror reflects the near-infrared (NIR) laser light but allows the blue 420 nm fluorescence light to pass through. A fluorescence concentrator, consisting of a lens doublet and a band-pass filter at 420 nm, is finally used to collect the fluorescence light onto a photomultiplier (PMT) while rejecting the detection of spurious NIR laser light. The collection efficiency, defined as the ratio between the number of blue photons that reach the PMT and number of blue photons generated in the cell through the two-photon process, is estimated to be close to 3 %. The resonance signal detected by the PMT is amplified with a high-gain transimpedance amplifier and fed to a lock-in amplifier to generate a dispersive zero-crossing error signal. This error signal is then used to generate a PID correction signal applied to the ECDL bias current, locking the laser to the atomic resonance frequency.

In parallel, a fraction of the laser output is coupled into an optical fiber and sent to an adjacent laboratory. There, it is used to detect a beatnote signal against a reference 778.1 nm signal delivered by a frequency-doubled, femtosecond-laser optical frequency comb (OFC) disciplined to an ultra low expansion (ULE) Fabry-Perot cavity stabilized laser. Long term drift due to the cavity is compensated with the help of the 100 MHz signal from a hydrogen maser. This drift control is performed

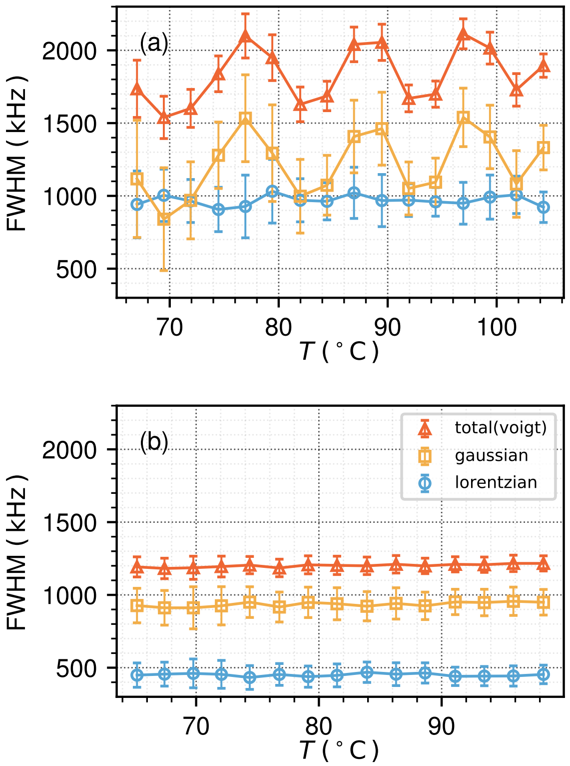

Fig. 3. Linewidth of the $F_g = 2$, $F_e = 4$ line of ^{87}Rb isotope versus the cell temperature, for the microfabricated cell in (a) and for a reference glass-blown evacuated Rb vapor cell in (b). The total linewidth, as well as Lorenztian and Gaussian linewidth contributions, have been estimated by fitting the lineshape of the resonance. Error bars, representing 2σ uncertainty, are extracted from the statistical distribution of 400 lineshape fits.

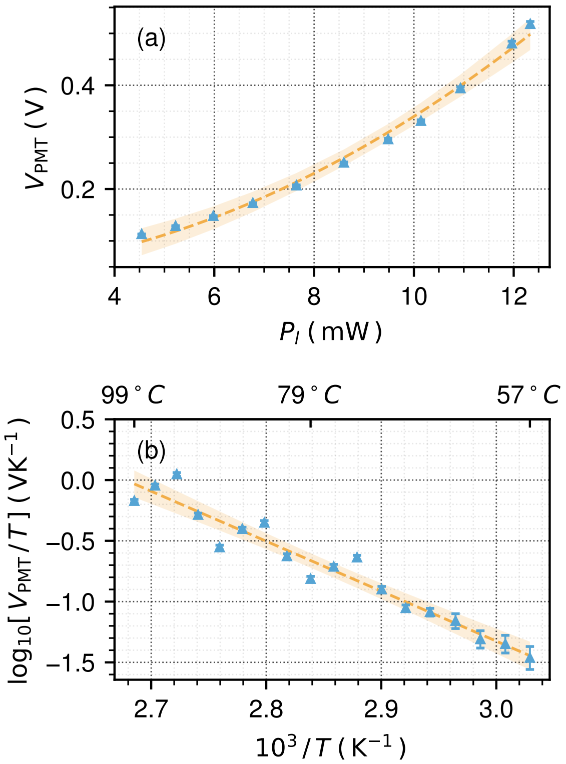

Fig. 4. Amplitude of the two-photon resonance versus the laser power P_l at the cell input (a) and the inverse of the cell temperature (b). For (a), the cell temperature was set to 110°C. A second order polynomial is used to fit experimental data. For (b), the laser power P_l was fixed to 12.3 mW. Eq. (1) is used to fit the data to the vapor pressure. The parameter A has been adapted to group together all offsets present in the logarithmic scale plot for a simplified interpretation. In contrast, the parameter B of Eq. (1) is used according to its original definition. The error bars and confidence intervals are drawn for 2σ uncertainty. The discrepancy observed at high temperatures can be explained by thermal effects in the MEMS cell holder (see Fig. 3).

with a phase-locked loop (PLL) that makes use of the OFC to realize the frequency division from the optical domain to the RF frequency range. With drift compensation, the cavity-based optical reference exhibits a short-term frequency stability of 2×10^{-15} at 1 s and below the 10^{-14} level at 10^4 s [49]. These performances are sufficient to ensure that frequency fluctuations of the beatnote are due to the microcell optical reference under test.

3. EXPERIMENTAL RESULTS

A. Features of the atomic resonance

Figure 2 shows the full spectrum of the $5S_{1/2} \rightarrow 5D_{5/2}$ transition at 778 nm of the Rb atoms in the microcell. Both ^{87}Rb and ^{85}Rb are present, with natural isotopic ratio. When hyperfine splitting is taken into account, absorption lines can be classified by the isotope and by the total angular momentum of the initial and final states of the transition, F_g and F_e. Among all these resonances, the $F_g = 3 \rightarrow F_e = 5$ line of the ^{85}Rb isotope (see Fig. 2(b)) is the most intense. This resonance is then best suited for optimizing the short-term frequency stability of the optical frequency reference [46]. However, the presence of contaminants in our cell, inducing line broadening of the optical resonances (see Fig. 3(a)), coupled to the close proximity of neighboring hyperfine levels, rendered the frequency lock of our laser sensitive to line pulling and frequency hopping, compromising its robustness against random disturbances. Thus, we have used the resonance with the second highest intensity, the $F_g = 2$, $F_e = 4$ line of the ^{87}Rb isotope (peak on the left of Fig. 2(a)), benefiting from a reduced overlap with neighboring lines.

Fitting the lineshape of the peaks in Fig. 2 reveals a Voigt line profile, which arises from a convolution of Lorenztian and Gaussian broadening components. The Lorentzian linewidth results from homogeneous broadening due to the natural linewidth of the transition, the collisional broadening induced by the presence of impurities in the cell [50], the rubidium pressure self-broadening [50] and the instantaneous linewidth of the laser [51]. The Gaussian linewidth results from inhomogenous broadening, mainly due to residual Doppler broadening caused by an imperfect overlap between the two counter-propagating beams of the Doppler-free scheme, but also from transit time broadening [52] and flicker of the laser frequency [51].

Figure 3(a) shows the total linewidth of the atomic resonance, as well as the Gaussian and Lorentzian widths, versus the cell temperature, in the MEMS cell. For comparison, data obtained in an evacuated glass-blown Rb vapor cell, of diameter 25 mm

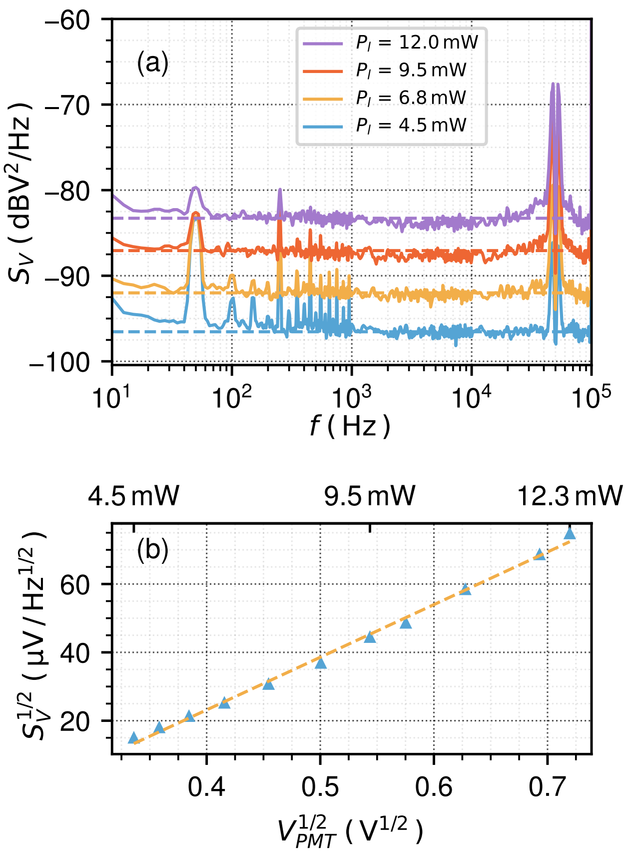

Fig. 5. (a) Total detection noise density spectra measured with a FFT analyzer at the output of the PMT for different laser powers at the cell input. Dashed horizontal lines are used to estimate the white noise floor. (b) Detection white noise density at the PMT output versus the square-root of the PMT output signal amplitude. The cell temperature is held constant at 110 °C.

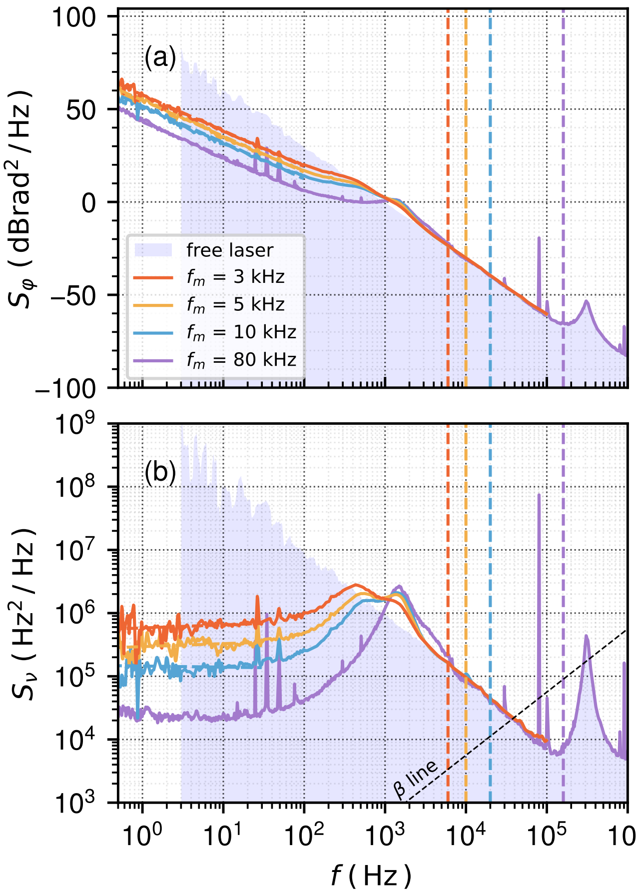

Fig. 6. (a) Absolute phase noise of the beatnote ($\sim$ 35 MHz) between the microcell-stabilized laser and the cavity-stabilized 778 nm reference signal, obtained for different laser modulation frequencies f_m. Vertical dashed lines are used to indicate $S_\varphi(2f_m)$. The shaded area shows the phase noise of the ECDL in the free-running regime (not locked to the microcell). (b) Frequency noise spectra, for the same conditions as in (a). The bump at $\sim$ 200 kHz is due to the ULE cavity servo loop. The shaded area shows the free-running frequency noise of the ECDL used in the TPA setup. The β separation line [51] is included for reference. Spectra were obtained using a phase noise analyzer (RS FSWP).

and length 70 mm, using the same beam size, are reported in Fig. 3(b). In the glass-blown cell, the Lorentzian width is about 450 kHz. This value is higher than the transition natural linewidth ($\sim$ 330 kHz). In this case, the main broadening contribution ($\sim$ 100 kHz) may be explained by the permeation of atmospheric helium ($\sim$ 4 mTorr) [50]. Smaller in magnitude, rubidium self-broadening ($\sim$ 18 kHz) and laser instantaneous linewidth ($\sim$ 19 kHz) also contribute to the overall Lorentzian linewidth. In the MEMS cell, the total linewidth is in the 1.5 - 2.1 MHz range. The Lorentzian width is about 950 kHz. This value, about 500 kHz higher than in the glass blown cell, is explained by the presence of additional impurities [53].

The Gaussian linewidth swings retrace across both increasing and decreasing temperature sweeps and are likely a result of incomplete cancellation of the Doppler effect, caused by misalignment between the counter-propagating laser beams. Notably, these oscillations are observed in the MEMS package but are absent in the glass-blown cell, suggesting that they are due to thermal expansion in the MEMS cell holder. With the same laser source and cell temperature, both the self-broadening and the laser broadening are the same across both cells. Significantly, transit time broadening ($\sim$ 150 kHz) is identical for both cells, enabling us to exclude this inhomogeneous contribution when estimating excess broadening due to MEMS cell impurities. For both types of cells, the Gaussian linewidth contribution is slightly increased with the rise of the cell temperature. We note that we did not observe any significant variation of the resonance linewidth with the laser intensity.

The amplitude of the atomic signal is correlated with both the intensity of the laser beam used to probe the transition and the rubidium vapor density. Two-photon absorption, being a second order nonlinear optical process, is proportional to the square of the incident laser intensity, provided that the atomic transition is not saturated. Additionally, the detection of 420 nm fluorescence is influenced by the branching ratio of the decay from the $5D_{5/2}$ excited state. This ratio must remain constant to ensure that the fluorescence signal is proportional to the two-photon absorption. This behaviour is well observed on Fig. 4(a). In light of these results, we have chosen to operate at P_l = 12.3 mW (the maximum available laser power in our setup) to get the best available signal to noise ratio.

On the other hand, the density of the rubidium vapor increases exponentially with temperature, as described by the simplified Antoine equation [54]

$$\log_{10} P_v = A - B/T\,, \tag{1}$$

where P_v is the vapor pressure, which can be related to the vapor density by means of the ideal gas law, T is the cell temperature and A and B are empirical parameters. Figure 4(b) shows the intensity of the atomic resonance, assumed to be proportional to the vapor density, and the fit to the Antoine equation. The value of B obtained from the fit of experimental data is $B_{\text{exp}} = -4100 \pm 260$ K , matching the reference value found in the literature ($B_{\text{ref}} = -4040 \pm 200$ K) [55]. Notably, the increase in fluorescence signal with increasing vapor pressure in Fig. 4 does not exhibit signs of reabsorption losses. The limited temperature range of this measurement was due to concerns about the thermal stability (thermal expansion) of the polyphenylene sulfide support holding the vapor cell physics package. Also at higher temperatures, i.e. beyond 130°C, reabsorption within the rubidium vapor is known to limit the fluorescence signal [52, 56]. Therefore, we chose to operate the cell at 110°C as a compromise to ensure the long-term mechanical stability of the setup while providing a high fluorescence intensity and then good short-term stability.

B. Main noise sources

B.1. Photon shot noise

Once we have assessed the influence of key experimental parameters on the resonance signal and linewidth, we can evaluate the main noise sources that affect the atomic resonance. Photon shot noise, originating from the quantization of light, is usually recognized as an important limiting factor to the short-term stability of optical standards based on TPA, due to the low absorption efficiency of this process. This type of noise exhibits white noise power spectral density (PSD) and a variance proportional to the light intensity. If this noise source dominates, the signal-to-noise ratio (SNR) is then directly proportional to the square root of the intensity of the signal. Furthermore, setting aside other sources of noise, the photodetector current noise PSD at the PMT cathode will be given by $S_i(f) = 2qI$, where q is the charge of the electron and I is the mean value of the photocurrent.

Figure 5(a) shows detection noise spectra measured at the output of the PMT transimpedance amplifier, for different values of the laser power at the cell input. We clearly observe a shift of the noise floor (white noise) following each increment in the laser power, together with a change in the amplitude of the frequency lock servo sidebands around 80 kHz. Derived from such spectra, Fig. 5(b) compares the detection noise floor S_v to the shot noise model (noise power $N \propto S^{1/2}$), revealing a shot noise limited signal.

B.2. Intermodulation effect

Another significant contribution to the short-term stability of passive continuous-wave optical frequency references is the intermodulation effect, induced by the frequency noise of the interrogating laser [47]. This short-term instability limit is given by Eq. (2), with $S_\nu(2f_m)$ the power spectral density of frequency fluctuations of the laser at twice the modulation frequency f_m, and ν_0 the clock transition frequency ($\nu_0 = 3.85 \times 10^{14}$ Hz in this case)

$$\sigma_y(\tau) \simeq \frac{1}{2}\sqrt{\frac{S_\nu(2f_m)}{\nu_0^2}}\,\frac{1}{\sqrt{\tau}}\,. \tag{2}$$

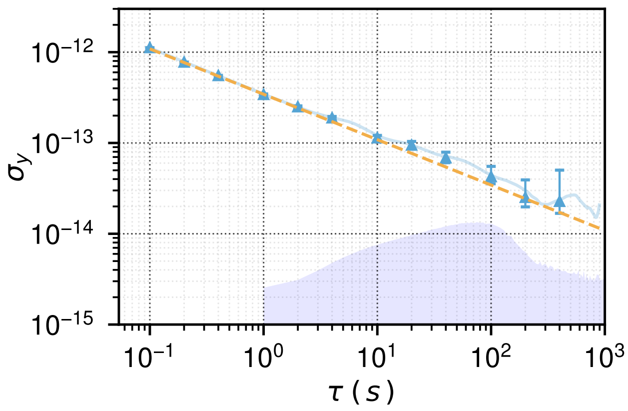

Fig. 7. Short-term fractional frequency stability of the microcell-stabilized laser, measured by beating its output signal against the reference cavity-stabilized 778 nm signal. The cell temperature is held constant at 110 °C, and the laser power P_l is equal to 12.3 mW. The shaded area shows the stability level of the cavity-stabilized reference. The microcell optical reference demonstrates a fractional Allan deviation of $3.5 \times 10^{-13}\ \tau^{-1/2}$ until 200 s (dashed line), averaging down to the low 10^{-14} range. A continuous line with the overlapping Allan deviation is also included. The value of $\sigma_y(1s)$ is consistent with the value reported in Fig. 8.

Figure 6 shows the phase noise (a) and frequency noise (b) spectrum of the ECDL used to probe the TPA resonance, in free-running and locked regimes. In the free-running case, the phase noise of the ECDL is about − 65 dBrad^2/Hz at f = 100 kHz, and ∼ 90 dBrad^2/Hz (10^9 rad^2/Hz) at f = 1 Hz. In the locked case, spectra were recorded for different values of the laser modulation frequency, f_m. Best results, obtained here with $f_m \simeq 80$ kHz, yield a phase noise of about + 43 dBrad^2/Hz at f = 1 Hz. Looking at Fig. 6(b), the frequency noise of the ECDL in the free-running case is about 6000 Hz^2/Hz at $f = 10^5$ Hz. With $f_m = 10^5$ Hz, the instability limit due to the intermodulation effect is then estimated at the level of 1.0×10^{-13} at 1 s. We also note on Fig. 6(b) that the laser frequency servo bandwidth is around 2 kHz. In addition to the main result, f_m = 80 kHz, three traces are shown for f_m =3, 5, 10 kHz (the f_m spikes have been removed for clarity). The effect of the intermodulation noise on the locked frequency noise is clear although it is not the limiting factor. We note that for these three measurements, the servo bandwidth was reduced by adjusting the PID controller.

C. Short-term frequency stability

We have measured the short-term fractional frequency stability of the microcell-stabilized ECDL. Corresponding results are reported in Fig. 7. The Allan deviation of the microcell reference is $\sigma_y(\tau) = 3.5 \times 10^{-13}\ \tau^{-1/2}$ until 200 s. This stability is approximately two times worse than the one reported in [46], in which the twice more intense $F_g = 3$, $F_e = 5$ line of ^{85}Rb isotope was used, and where the minimum laser frequency noise was slightly lower (5×10^3 Hz^2/Hz). Hence, these results confirm the potential of this spectroscopic approach for the advancement of ultra-stable microcell-stabilized optical frequency references.

The SNR-limited short-term stability of the optical microcell

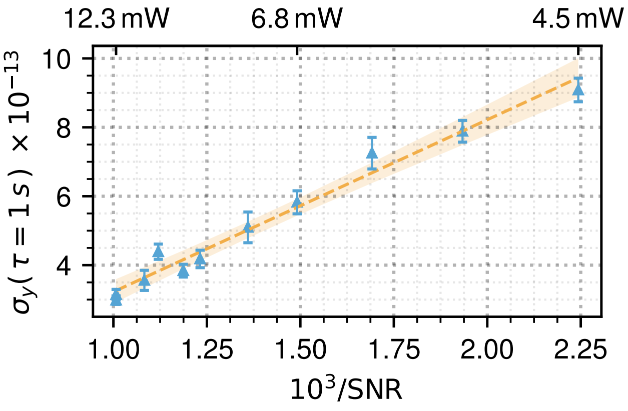

Fig. 8. Short-term stability at 1 s of the microcell-stabilized reference versus 1/SNR. The cell temperature is held constant at 110 °C, the amplitude SNR values (evaluated in a 1 Hz bandwidth) are the same as those in Fig. 5, and are obtained by changing the laser power, as shown in the top x-axis. Experimental data are fitted to Eq. (3), showing a good agreement with the SNR-limited noise model. The error bars and confidence intervals are drawn to represent the 2σ uncertainty.

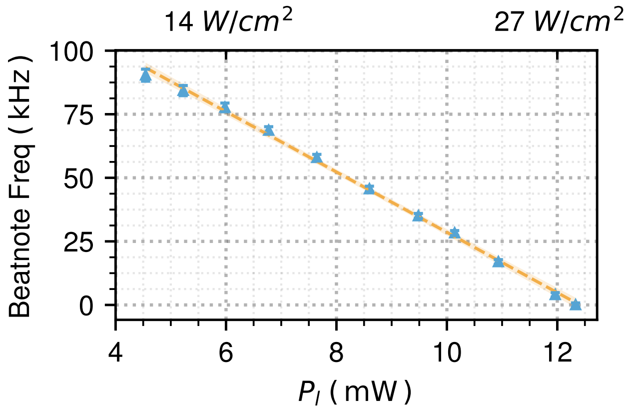

Fig. 9. Dependence of the microcell reference frequency to the laser power at the cell input, P_l. Estimation of the laser intensity is indicated as a second top x-axis. Experimental data are fitted by a linear function, with a slope of $-$ 11.9 ± 0.3 kHz/mW. The cell temperature is held constant at 110 °C. Error bars and confidence intervals are drawn to represent the 2σ uncertainty.

reference can be approximated by:

$$\sigma_y(\tau) \simeq \eta \frac{\Delta\nu}{\nu_0} \frac{S_v}{S} \frac{1}{\sqrt{2\tau}} \tag{3}$$

where η is a semi-empirical term [57, 58] representing the linearized response of the feedback scheme, $\Delta\nu$ is the resonance linewidth ($\sim$ 1.5 MHz), S is the resonance signal power, S_v is the detection noise amplitude density and τ is the integration time. We measured the 2f modulation response of the PMT [59] to calculate the SNR of the resonance signal, allowing the simultaneous measurement of the white noise in the PMT signal. The SNR was calculated as S/N, where N is the total noise power evaluated for a 1 Hz bandwidth, as illustrated in Fig. 5. Simultaneously with the SNR measurement, we used a frequency counter to measure the beatnote frequency between the microcell reference and the comb. The agreement between the measurements and Eq. (3), illustrated by the linear fit of the stability at 1 s as a function of 1/SNR in Fig. 8, confirms that the short-term frequency stability of the microcell optical standard is currently limited by the SNR, at all laser power values. In addition, the value of the slope of the linear fit, equal to $m = 5.0 \pm 0.2 \times 10^{-10}$, can be used to estimate the value $\eta = 0.17 \pm 0.01$. This value is close to the value $\eta \simeq 0.2$ typically obtained when using the lock-in amplifier output to measure the power of the resonance signal [58].

D. Light-shift

Beyond 200-300 seconds of integration time, a degradation of the microcell reference stability was typically observed. Since light-shift effects have been identified in several studies as an important contribution to the mid-term and long-term stability of TPA-based optical cell clocks [42, 43, 45], we have, in the last part, measured the dependence of the microcell reference frequency to variations of the laser power at the cell input. Results are illustrated in Fig. 9.

Experimental data are well-fitted by a linear sensitivity coefficient of $-$ 11.9 ± 0.3 kHz/mW, i.e. -3.1×10^{-11}/mW in fractional value. This coefficient indicates that fluctuations of the laser power should be reduced at a level lower than $3.2\times\ 10^{-5}$ mW to reach a stability level of 10^{-15}. Light-shift mitigation techniques might be also implemented to reduce the light-shift coefficient [60–62]. Variations on the pointing direction of the laser beam could also induce a random, time-dependent light shift proportional to the intensity of the laser light. The reduction of collisional shifts, sensitive to cell temperature fluctuations, will also require careful attention. These studies remain out of the scope of the paper and will be performed in a future work.

4. CONCLUSIONS

We have reported the development and short-term stability characterization of an external-cavity diode laser stabilized on a microfabricated vapor cell using spectroscopy of the Rb 778 nm two-step transition. The impact of some key experimental parameters (laser power, cell temperature) on the sub-Doppler resonance features (signal and linewidth) was reported. The microcell-stabilized laser demonstrates an Allan deviation of $3.5 \times 10^{-13}\ \tau^{-1/2}$, reaching 2×10^{-14} at 200 s. The laser short-term instability is in good agreement with the resonance signal-to-noise ratio and is currently limited by the photon shot noise. It could be improved with increased laser power or cell temperature. The contribution of the intermodulation effect, induced by the free-running laser frequency noise (6000 $\mathrm{Hz}^2/\mathrm{Hz}$ at f = 1.6 × 10^5 Hz), is evaluated at the level of 1×10^{-13} at 1 s. Various paths of optimization, such as the development of microcells with enhanced purity [32, 63] for the detection of narrower resonances, the optimization of the fluorescence collection and the use of the more intense $5S_{1/2}(F=3) \rightarrow 5D_{5/2}(F=5)$ transition of ^{85}Rb atom [46] for atomic signal enhancement, or the use of lasers with lower frequency noise [64, 65], might be explored in the future for improvement of the microcell reference short-term stability. Studies will be also engaged to mitigate main frequency shifts and improve the mid-term and long-term stability of the optical standard.

FUNDING

European Defence Fund (EDF-2021-DIS-RDISADEQUADE); Agence Nationale de la Recherche (ANR 10-LABX-48-01, ANR 11-EQPX-0033, ANR-17-EURE-0002); Centre National d'Etudes Spatiales (200837/00).

ACKNOWLEDGMENTS

This work was funded by the European Union. Views and opinions expressed are, however, those of the author(s) only and do not necessarily reflect those of the European Union. Neither the European Union nor the granting authority can be held responsible for them. This project has received funding from the European Defence Fund (EDF) under grant agreement EDF-2021-DIS-RDIS-ADEQUADE. This work was also funded by Agence Nationale de la Recherche (ANR 10-LABX-48-01, ANR 11- EQPX-0033, ANR-17-EURE-0002) and Centre National d'Etudes Spatiales (200837/00). The authors would like to thank V. Giordano and M. Abdel Hafiz for careful reading of the manuscript and M. Hauden for his valuable input.

DISCLOSURES

The authors declare no conflicts of interest.

DATA AVAILABILITY STATEMENT

The data that support the findings of this study are available from the corresponding author upon reasonable request.

REFERENCES

1. J. Kitching, S. Knappe and L. Hollberg, Miniature vapor-cell atomic-frequency refereces, Appl. Phys. Lett. **81,** 3, 553-555 (2002).
2. C. Affolderbach, A. Nagel, S. Knappe, C. Jung, D. Wiedenmann and R. Wynands, Non-linear spectroscopy with a vertical-cavity surface-emitting laser, Appl. Phys. B **70,** 407-413 (2000).
3. S. Knappe, V. Shah, P.D.D. Schwindt, L. Hollberg, J. Kitching, L. A. Liew and J. Moreland, A microfabricated atomic clock, Appl. Phys. Lett. **85,** 9, 1460-1462 (2004).
4. E. Arimondo, Coherent population trapping in laser spectroscopy, Progress in Optics **35**, 257 (1996).
5. N. Cyr, M. Tetu, M. Breton, All-optical microwave frequency standard: a proposal, IEEE Trans. Instr. Meas. **42,** 640-649 (1993).
6. M. Stahler, R. Wynands, S. Knappe, J. Kitching, L. Hollberg, A. Taichenachev and V. Yudin, Coherent population trapping resonances in thermal ^{85}Rb vapor: D$_1$ versus D$_2$ line excitation, Opt. Lett. **27,** 16, 1472-1474 (2002).
7. D. K. Serkland, K. M. Geib, G. M. Peake, R. Lutwak, A. Rashed, M. Varghese, G. Tepolt and M. Prouty, VCSELs for atomic sensors, Proc. SPIE **6484,** Vertical-Cavity Surface-Emitting Lasers XI, 648406 (2007).
8. A. Al-Samaneh, M. Bou Sanayeh, M. J. Miah, W. Schwarz, D. Wahl, A. Kern and R. Michalzik, Polarization-stable vertical-cavity surface-emitting lasers with inverted grating relief for use in microscale atomic clocks, Appl. Phys. Lett. **101,** 171104 (2012).
9. E. Kroemer, J. Rutkowski, V. Maurice, R. Vicarini, M. Abdel Hafiz, C. Gorecki and R. Boudot, Characterization of commercially vertical-cavity surface-emitting lasers tuned on Cs D$_1$ line at 894.6 nm for atomic clocks, Appl. Opt. **55,** 31, 8839-8847 (2016).
10. S. Knappe, V. Gerginov, P.D.D. Schwindt, V. Shah, H. G. Robinson, L. Hollberg and J. Kitching, Atomic vapor cells for chip-scale atomic clocks with improved long-term frequency stability, Opt. Lett. **30,** 18, 2351-2353 (2005).
11. A. Douahi, L. Nieradko, J. C. Beugnot, J. Dziuban, H. Maillotte, S. Guerandel, M. Moraja, C. Gorecki and V. Giordano, Vapour microcell for chip scale atomic frequency standard, Elec. Lett. **43,** 5, 33-34 (2007).
12. L-A. Liew, J. Moreland and V. Gerginov, Wafer-level filling of microfabricated atomic vapor cells based on thin-film deposition and photolysis of cesium azide, Appl. Phys. Lett. **90,** 114106 (2007).
13. M. Hasegawa, R. K. Chutani, C. Gorecki, R. Boudot, P. Dziuban, V. Giordano, S. Clatot, J. Dziuban and L. Mauri, Microfabrication of cesium vapor cells with buffer gas for MEMS atomic clocks, Sensors Actuators A - Phys. **167,** 594-601 (2011).
14. S. Karlen, J. Gobet, T. Overstolz, J. Haesler and S. Lecomte, Lifetime assessment of RbN$_3$-filled MEMS atomic vapor cells with Al$_2$O$_3$ coating, Opt. Exp. **25,** 3, 2187-2194 (2017).
15. V. Maurice, J. Rutkowski, E. Kroemer, S. Bargiel, N. Passilly, R. Boudot, C. Gorecki, L. Mauri and M. Moraja, Microfabricated vapor cells filled with a cesium dispensing paste for miniature atomic clocks, Appl. Phys. Lett. **110,** 164103 (2017).
16. V. Maurice, C. Carlé, S. Keshavarzi, R. Chutani, S. Queste, L. Gauthier-Manuel, J. M. Cote, R. Vicarini, R. Boudot and N. Passilly, Wafer-level vapor cells filled with laser-actuated hermetic seals for integrated atomic devices, Microsystems and Nanoengineering **8,** 129 (2022).
17. R. Vicarini, V. Maurice, M. Abdel Hafiz, J. Rutkowski, C. Gorecki, N. Passilly, L. Ribetto, V. Gaff, V. Volant, S. Galliou and R. Boudot, Demonstration of the mass-producible feature of a Cs vapor microcell technology for miniature atomic clocks, Sensors Actuators: Phys. A **280,** 99-106 (2018).
18. D. G. Bopp, V. M. Maurice and J. E. Kitching, Wafer-level fabrication of alkali vapor cells using in-situ atomic deposition, J. Phys. Photonics **3,** 015002 (2021).
19. Y. Z. Zhao, S. Tanner, A. Casagrande, C. Affolderbach, L. Schneller, G. Mileti and P-A. Farine, CPT cesium-cell atomic clock operation with a 12-mW frequency synthesizer ASIC, IEEE Trans. Instr. Meas. **64,** 1, 263-270 (2014).
20. R. Lutwak, A. Rashed, M. Varghese, G. Tepolt, J. LeBlanc, M. Mescher, D. K. Serkland, K. M. Geib, G. M. Peake and S. Romisch, The chip-scale atomic clock - Prototype evaluation, in Proceeding of Precise Time and Time Interval (PTTI) Meeting (2007), pp. 269–290.
21. J. Haesler, L. P. Balet, S. Karlen, T. Overstolz, B. Gallinet, S. Lecomte, F. Droz, K. Kautio, P. Karioja, M. Lahti, A. Maathanen, O. Lahtinen, V. Hevonkorpi, Low-power and low-profile miniature atomic clock ceramic based flat form factor miniature atomic clock physics package (C-MAC), In Proceedings of Joint Conference of the European Frequency and Time Forum and IEEE International Frequency Control Symposium (EFTF/IFCS), Besancon, France (2017).
22. J. Kitching, Chip-scale atomic devices, Appl. Phys. Rev. **5,** 031302 (2018).
23. H. Zhang, H. Hans, N. Tharayil, A. Shirane, M. Suzuki, K. Harasaka, K. Adachi, S. Goka, S. Yanagimachi and K. Okada, ULPAC: A miniaturized ultra-low power atomic clock, IEEE Journ. Solid State Circuits **54,** 11, 3135-3148 (2019).
24. S. Yanagimachi, K. Harasaka, R. Suzuki, M. Suzuki and S. Goka, Reducing frequency drift caused by light shift in coherent population trapping-based low-power atomic clocks, Appl. Phys. Lett. **116,** 104102 (2020).
25. C. Carlé, M. Abdel Hafiz, S. Keshavarzi, R. Vicarini, N. Passilly, and R. Boudot, A pulsed-CPT Cs-Ne microcell atomic clock with frequency stability below 2×10^{-12} at 10^5 s, Opt. Exp. **31,** 5, 8160-8169 (2023).
26. M. Abdel Hafiz, C. Carlé, N. Passilly, JM. Danet, C. E. Calosso and R. Boudot and , Light-shift mitigation in a microcell-based atomic clock with symmetric auto-balanced Ramsey spectroscopy, Appl. Phys. Lett. **120,** 064101 (2022).
27. A. T. Dellis, V. Shah, E. A. Donley, S. Knappe and J. Kitching, Low helium permeation cells for atomic microsystems technology, Opt. Lett. **41,** 12, 2775-2778 (2016).
28. C. Carlé, S. Keshavarzi, A. Mursa, P. Karvinen, R. Chutani, S.

Bargiel, S. Queste, R. Vicarini, P. Abbé, M. Abdel Hafiz, V. Maurice, R. Boudot and N. Passilly, Reduction of helium permeation in microfabricated cells using aluminosilicate glass substrates and Al_2O_3 coatings, J. Appl. Phys. **133,** 214501 (2023).

29. O. Kozlova and S. Guérandel and E. de Clercq, Temperature and pressure shift of the Cs clock transition in the presence of buffer gases: Ne, N_2, Ar, Phys. Rev. A **83,** 062714 (2011).
30. S. Micalizio, C. E. Calosso, A. Godone and F. Levi, Metrological characterization of the pulsed Rb clock with optical detection, Metrologia **49,** 4, 425-436 (2012).
31. E. Batori, C. Affolderbach, M. Pellaton, F. Gruet, M. Violetti, Y. Su, A. K. Skrivervik and G. Mileti, μ-POP clock: A microcell atomic clock based on double-resonance Ramsey scheme, Phys. Rev. Appl. **18,** 054039 (2022).
32. G. Martinez, C. Li, A. Staron, J. Kitching, C. Raman and W. McGehee, A chip-scale atomic beam clock, Nature Commun. **14,** 3501 (2023).
33. M. T. Hummon, S. Kang, D. G. Bopp, Q. Li, D. A. Westly, S. Kim, C. Fredrick, S. A. Diddams, K. Srinivasan, V. Aksyuk and J. E. Kitching, Photonic chip for laser stabilization to an atomic vapor with 10^{-11} instability, Optica **5,** 443-449 (2018).
34. A. Strangfeld, S. Kanthak, M. Schiemangk, B. Wiegand, A. Wicht, A. Ling and M. Krutzik, Prototype of a compact rubidium-based optical frequency reference for operation on nanosatellites, J. Opt. Soc. Am. B **38,** 6, 1885-1890 (2021).
35. A. Strangfeld, B. Wiegand, J. Kluge, M. Schoch and M. Krutzik, Compact plug and play optical frequency reference device based on Doppler-free spectroscopy of rubidium vapor, Opt. Express **30,** 12039-12047 (2022).
36. M. Abdel Hafiz, G. Coget, E. de Clercq and R. Boudot, Doppler-free spectroscopy on the Cs D_1 line with a dual-frequency laser, Opt. Lett. **41,** 2982-2985 (2016).
37. D. V. Brazhnikov, M. Petersen, G. Coget, N. Passilly, V. Maurice, C. Gorecki and R. Boudot, Dual-frequency sub-Doppler spectroscopy: extended theoretical model and microcell-based experiments, Phys. Rev. A **99,** 062508 (2019).
38. A. Gusching, J. Millo, I. Ryger, R. Vicarini, M. Abdel Hafiz, N. Passilly and R. Boudot, Cs microcell optical reference with frequency stability in the low 10^{-13} range at 1 s, Opt. Lett. **48,** 6, 1526-1529 (2023).
39. F. Nez, F. Biraben, R. Felder and Y. Millerioux, Optical frequency determination of the hyperfine components of the $5S_{1/2}$-$5D_{3/2}$ two-photon transitions in rubidium, Opt. Commun. **102,** 432-438 (1993).
40. V. Gerginov and K. Beloy, Two-photon optical frequency reference with active ac Stark shift cancellation, Phys. Rev. Appl. **10,** 014031 (2018).
41. C. Perrella, P.S. Light, J.D. Anstie, F.N. Baynes, R.T. White, and A.N. Luiten, Dichroic two-photon rubidium frequency standard, Phys. Rev. Appl. **12,** 054063 (2019).
42. K. W. Martin, G. Phelps, N. D. Lemke, M. S. Bigelow, B. Stuhl, M. Wojcik, M. Holt, I. Coddington, M. W. Bishop, and J. H. Burke, Compact optical atomic clock based on a two-photon transition in rubidium, Phys. Rev. Appl. **9,** 014019 (2018).
43. N. D. Lemke, K. W. Martin, R. Beard, B. K. Stuhl, A. J. Metcalf and J. D. Elgin, Measurement of optical rubidium clock frequency spanning 65 days, Sensors **22,** 1982 (2022).
44. Z. L. Newman, V. Maurice, T. Drake, J. R. Stone, T. C. Briles, D. T. Spencer, C. Fredrick, Q. Li, D. Westly, B. R. Ilic, B. Shen, M.-G. Suh, K. Y. Yang, C. Johnson, D. M. S. Johnson, L. Hollberg, K. J. Vahala, K. Srinivasan, S. A. Diddams, J. Kitching, S. B. Papp, and M. T. Hummon, Architecture for the photonic integration of an optical atomic clock, Optica **6,** 680-685 (2019).
45. V. Maurice, Z. L. Newman, S. Dickerson, M. Rivers, J. Hsiao, P. Greene, M. Mescher, J. Kitching, M. T. Hummon and C. Johnson, Miniaturized optical frequency reference for next-generation portable optical clocks, Opt. Express **28,** 24708-24720 (2020).
46. Z. L. Newman, V. Maurice, C. Fredrick, T. Fortier, H. Leopardi, L. Hollberg, S. A. Diddams, J. Kitching, and M. T. Hummon, High-performance, compact optical standard, Opt. Lett. **46,** 18, 4702-4705 (2021).
47. C. Audoin, V. Candelier and N. Dimarcq, A limit to the frequency stability of passive frequency standards due to an intermodulation effect, IEEE Trans. Instr. Meas. **40,** 2, 121-125 (1991).
48. F. Tricot, D. H. Phung, M. Lours, S. Guérandel and E. de Clercq, Power stabilization of a diode laser with an acousto-optic modulator, Rev. Sci. Instr. **89,** 113112 (2018).
49. A. Didier, J. Millo, S. Grop, B. Dubois, E. Bilger, E. Rubiola, C. Lacroute and Y. Kersalé, Ultra-low phase noise all-optical microwave generation setup based on commercial devices, Appl. Opt. **54,** 12, 3682-3686 (2015).
50. N. D. Zameroski, G. D. Hager, C. J. Erickson and J. H. Burke, Pressure broadening and frequency shift of the $5S_{1/2} \rightarrow 5D_{5/2}$ and $5S_{1/2} \rightarrow 7S_{1/2}$ two photon transitions in 85Rb by the noble gases and N2, J. Phys. B: At. Mol. Opt. Phys. **47,** 225205 (2014).
51. G. Di Domenico, S. Schilt and P. Thomann, Simple approach to the relation between laser frequency noise and laser line shape, Appl. Opt. **49,** 4801-4807 (2010).
52. K. Hassanin, P. Federsel, F. Karlewski, and C. Zimmermann, 55S-5D two-photon transition in rubidium vapor at high densities, Phys. Rev. A **107,** 043104 (2023).
53. M. Hasegawa, R. K. Chutani, R. Boudot, L. Mauri, C. Gorecki, X. Liu and N. Passilly, Effects of getters on hermetically-sealed micromachined cesium-neon cells for atomic clocks, J. MicroMec. Microeng. **23,** 055022 (2013).
54. G. Thomson, The Antoine equation for vapor-pressure data, Chemical Reviews, **38,** 1, 1-39 (1946).
55. C. B. Alcock, V. P. Itkin and M. K. Horrigan, Vapour Pressure Equations for the Metallic Elements: 298–2500K, Canadian Metallurgical Quarterly, **23,** 3, 309-313 (1984).
56. A. J. Olson, E. J. Carlson and S. K. Mayer, Two-photon spectroscopy of rubidium using a grating-feedback diode laser, Am. J. Phys. **74,** 3, 218-223 (2006).
57. J. Vanier and C. Audoin, The quantum physics of atomic frequency standards, Adam-Hilger, CRC Press (1989).
58. J. Vanier and L. G. Bernier, On the signal-to-noise ratio and short-term stability of passive rubidium frequency standards, IEEE Trans. on Instr. and Meas. **30**, 277-282 (1981).
59. A. Hangauer, J. Chen, R. Strzoda and M. C. Amann, Multi-harmonic detection in wavelength modulation spectroscopy systems, Applied Physics B, **110**, 177-185, (2012)
60. V. I. Yudin, M. Yu Basalaev, A. V. Taichenachev, J. W. Pollock, Z. L. Newman, M. Shuker, A. Hansen, M. T. Hummon, R. Boudot, E. A. Donley and J. Kitching, General methods for suppressing the light shift in atomic clocks using power modulation, Phys. Rev. Appl. **14,** 024001 (2020).
61. M. Abdel Hafiz, R. Vicarini, N. Passilly, C. E. Calosso, V. Maurice, J. W. Pollock, A. V. Taichenachev, V. I. Yudin, J. Kitching and R. Boudot, Protocol for light-shift compensation in a continuous-wave microcell atomic clock, Phys. Rev. Appl. **14,** 034014 (2020).
62. D. Li, K. Liu, P. Wang and S. Kang, Dual-interrogation method for suppressing light shift in Rb 778 nm two-photon transition optical frequency standard, Opt. Express **32,** 2, 2766-2773 (2024).
63. R. Boudot, J. P. McGilligan, K. R. Moore, V. Maurice, G. D. Martinez, A. Hansen, E. de Clercq and J. Kitching, Enhanced observation time of magneto-optical traps using micro-machined non-evaporable getter pumps, Sci. Rep. **10,** 16590 (2020).
64. J. Guo et al., Chip-based laser with 1-hertz integrated linewidth, Sci. Adv. **8,** eabp9006 (2022).
65. M. Clementi et al., A chip-scale second-harmonic source via self-injection-locked all-optical poling, Light Science and Applications **12,** 296 (2023).